

**Jason W. Middleton, André Longtin, Jan Benda and Leonard Maler**

*J Neurophysiol* 101:1160-1170, 2009. First published Dec 17, 2008; doi:10.1152/jn.90814.2008

**You might find this additional information useful...**

---

This article cites 53 articles, 27 of which you can access free at:

<http://jn.physiology.org/cgi/content/full/101/3/1160#BIBL>

This article has been cited by 1 other HighWire hosted article:

**Transient Signals Trigger Synchronous Bursts in an Identified Population of Neurons**

G. Marsat, R. D. Proville and L. Maler

*J Neurophysiol*, August 1, 2009; 102 (2): 714-723.

[\[Abstract\]](#) [\[Full Text\]](#) [\[PDF\]](#)

Updated information and services including high-resolution figures, can be found at:

<http://jn.physiology.org/cgi/content/full/101/3/1160>

Additional material and information about *Journal of Neurophysiology* can be found at:

<http://www.the-aps.org/publications/jn>

---

This information is current as of September 22, 2009 .

# Postsynaptic Receptive Field Size and Spike Threshold Determine Encoding of High-Frequency Information Via Sensitivity to Synchronous Presynaptic Activity

Jason W. Middleton,<sup>1,2</sup> André Longtin,<sup>1,2,3</sup> Jan Benda,<sup>4</sup> and Leonard Maler<sup>1,2</sup>

<sup>1</sup>Departments of Cellular and Molecular Medicine <sup>3</sup>Physics and <sup>2</sup>Centre for Neural Dynamics, University of Ottawa, Ottawa, Ontario, Canada; and <sup>4</sup>Institute for Theoretical Biology, Humboldt University, Berlin, Germany

Submitted 25 July 2008; accepted in final form 11 December 2008

**Middleton JW, Longtin A, Benda J, Maler L.** Postsynaptic receptive field size and spike threshold determine encoding of high-frequency information via sensitivity to synchronous presynaptic activity. *J Neurophysiol* 101: 1160–1170, 2009. First published December 17, 2008; doi:10.1152/jn.90814.2008. Parallel sensory streams carrying distinct information about various stimulus properties have been observed in several sensory systems, including the visual system. What remains unclear is why some of these streams differ in the size of their receptive fields (RFs). In the electrosensory system, neurons with large RFs have short-latency responses and are tuned to high-frequency inputs. Conversely, neurons with small RFs are low-frequency tuned and exhibit longer-latency responses. What principle underlies this organization? We show experimentally that synchronous electroreceptor afferent (P-unit) spike trains selectively encode high-frequency stimulus information from broadband signals. This finding relies on a comparison of stimulus-spike output coherence using output trains obtained by either summing pairs of recorded afferent spike trains or selecting synchronous spike trains based on coincidence within a small time window. We propose a physiologically realistic decoding mechanism, based on postsynaptic RF size and postsynaptic output rate normalization that tunes target pyramidal cells in different electrosensory maps to low- or high-frequency signal components. By driving realistic neuron models with experimentally obtained P-unit spike trains, we show that a small RF is matched with a postsynaptic integration regime leading to responses over a broad range of frequencies, and a large RF with a fluctuation-driven regime that requires synchronous presynaptic input and therefore selectively encodes higher frequencies, confirming recent experimental data. Thus our work reveals that the frequency content of a broadband stimulus extracted by pyramidal cells, from P-unit afferents, depends on the amount of feedforward convergence they receive.

## INTRODUCTION

Many sensory systems have inputs topographically mapped onto target cells the tuning curves, or receptive fields (RFs), of which are sensitive to different features of sensory input. Theoretical studies have concluded that for a two-dimensional input space, estimation of location parameters is independent of RF size (Abbott and Dayan 1999; Zhang and Sejnowski 1999). Optimal estimation of parameters such as stimulus intensity and spread are dependent on RF size (Lewis and Maler 2001), and this might be related to experimentally reported variations of RF size (or tuning curve width) in various sensory systems (see following text). These studies do

not, however, take into account temporal response properties that also appear to correlate with RF size. In the mammalian visual system, larger RF size is correlated with shorter response latencies in retina (Wässle 2004), LGN (Weng et al. 2005), and cortex (Malone et al. 2007).

This correlation was also observed in the electrosensory system where cells with large RFs had the shortest latency response and were also tuned to the highest temporal frequencies (Shumway 1989). We demonstrate that RF size and concomitant changes in spike threshold directly determine the frequency response characteristics of sensory neurons; frequency tuning requirements might therefore account for much of the observed variation in RF size.

The weakly electric fish *Apteronotus leptorhynchus* probes its environment by emitting an oscillatory electric field, the electric organ discharge (EOD). Amplitude modulations (AMs) of this self-generated field arise in a natural context from both nearby objects and communication signals and are detected by cutaneous electroreceptors (P-units). The electrosensory lateral line lobe (ELL) of the weakly electric fish has three topographic maps (segments) of the body surface containing pyramidal cells that receive convergent P-unit input. Also, the maps display different anatomical and physiological properties: the lateral segment (LS) has large RFs and is responsive to high-frequency AMs, whereas the centromedial segment (CMS) has small RFs (Shumway 1989) and is tuned to low frequencies (Krahe et al. 2008). Cells in the centrolateral segment (CLS) have anatomical and physiological properties intermediate to those of the CMS and LS (Krahe et al. 2008); however, their behavioral role is not known. We will focus on the two extreme maps (CMS and LS), which have been implicated in different behavioral functions (Metzner and Juranek 1997).

Here we demonstrate that synchronous P-unit activity selectively codes for the high-frequency components of broadband sensory inputs. We then use pyramidal cell models, taking into account the observed covariance of pyramidal cell RF size and biophysical single-cell properties, to show how a simple decoding mechanism, involving both extensive afferent convergence and a high spike response threshold (controlling output rate), can selectively extract the synchronous spikes from a population of afferents containing both synchronous and asynchronous spikes. In the electrosensory system, this further

Present address and address for reprint requests and other correspondence: J. W. Middleton, Dept. of Neurobiology, University of Pittsburgh School of Medicine, 200 Lothrop St., BST E1407, Pittsburgh, PA 15261 (E-mail: jmiddlet@pitt.edu).

The costs of publication of this article were defrayed in part by the payment of page charges. The article must therefore be hereby marked “advertisement” in accordance with 18 U.S.C. Section 1734 solely to indicate this fact.

implies that this decoding mechanism will extract the high-frequency information transmitted by synchronous P-unit spikes; the same mechanism might, in other systems, be used to extract any stimulus encoded by spike synchrony (Benda et al. 2006). Using coherence as a response measure, we show qualitative agreement between the responses of our models and recent experimentally observed ELL pyramidal cell responses (Krahe et al. 2008). By isolating and varying model parameters, we elucidate the mechanistic link between the synchronous activity we measure in P-units and the previously observed responses of pyramidal cells. While we do not know of a way to directly manipulate spike threshold in pyramidal cells, the natural variation of this parameter across sensory maps makes the electrosensory system ideal for studying this problem.

Our results may help understand a general coding scheme whereby a parallel processing in the temporal and frequency domains occurs across different sensory maps based on their different RF sizes and spike thresholds. This type of processing, mediated by synchrony, varying levels of convergence, and threshold regulation, may also occur in other sensory systems, whether or not the distinct maps are co-extensive, as in the X and Y ganglion cells of the retina (Wässle 2004), or anatomically segregated, as in the electrosensory system. It should be noted that this is just one example of the many forms of “parallel” information streams in sensory systems. The magno- and parvocellular streams in the primate visual system are preferentially sensitive to luminance contrast and color, respectively (Kaplan and Shapley 1982). In the (whisker) somatosensory system of rodents, a form of parallelization is hypothesized whereby the lemniscal and paralemniscal pathways encode information about whisker contacts with external objects and self-generated whisker kinematics, respectively (Alloway 2008).

The similarity of frequency selectivity of synchronous pre-synaptic activity and the frequency selectivity of the postsynaptic cell, dependent on its RF structure, remains to be confirmed in other sensory systems.

## METHODS

### Electrophysiology

Single P-unit recordings were made from the posterior branch of the anterior lateral line nerve ganglion; this contains only electroreceptor afferent fibers innervating electroreceptors on the fish's trunk (Maler et al. 1974). For surgical exposure of the trunk nerve, fish were anesthetized (Tricaine-S; Western Chemical, Ferndale, WA). After surgery, fish were immobilized (pancuronium bromide; Sabex, Boucherville, Quebec, Canada) and transferred into a tank (28°C) where they were respired by a constant flow of oxygenated water through the mouth. Action potentials from single P-unit afferents were recorded in vivo with sharp glass micropipettes (100–140 MΩ) that were advanced into the nerve with piezoelectric microdrives (Inchworm IW-711, Burlington, Fishers, NY; and MM3A, Kleindiek nanotechnology). The potential between the micropipette and the reference electrode, which was placed on the nerve close to the electrode, was amplified (Axoclamp 2 A; Axon Instruments, Union City, CA), band-pass filtered (0.45–7 kHz; PC1; TDT, Alachua, FL), and notch filtered at 60 Hz and the fish's EOD frequency (Ultra-Q Pro; Behringer, Willich, Germany). All experimental protocols were approved by the University of Ottawa Animal Care Committee.

The EOD, unperturbed by the stimulus, was recorded between the head and tail of the fish using two vertical carbon rods (11 cm long,

8 mm diam). A window discriminator (SD1; TDT) was used to detect the EOD zero-crossing times. TTL pulses occurring at the EOD zero-crossing times were used to drive a waveform generator (40 MS/s; Wavetek-Datron, Everett, WA) in sine-wave-triggered mode, thereby creating a mimic of the fish's EOD. This EOD mimic was used as a carrier to deliver the stimulus as an AM of the fish's own EOD. The stimulus, a Gaussian-distributed random process with a frequency cutoff of 300 Hz, was multiplied with the EOD mimic, isolated (Model 2002; A-M Systems, Carlsborg, WA), and delivered by two stimulation electrodes (30 cm long, 8-mm-diam carbon rods) placed 10 cm on either side of the fish, parallel to its longitudinal axis. This method of modulating the EOD amplitude adds (or subtracts) the stimulus waveform from the baseline EOD without concurrent frequency modulations (FMs). This stimulation geometry does not affect the head-tail EOD recording due to the orthogonal alignment of stimulation electrodes. A 5-s-long signal was presented, and all analysis used only the final 4 s of stimulation to avoid effects of response transients. We chose the 0- to 300-Hz range because this is approximately the maximal beat frequency range expected for these fish. Because females often have EOD frequencies as low as 700 Hz and males can reach 1,000 Hz, this may lead to beat frequencies as high as 300 Hz.

P-units are sensitive to transdermal electrical gradients; instead of recording the transdermal potential directly (Chen et al. 2005), we obtained a surrogate of this measure by recording the potential between two silver wires coated with nail polish, 1 cm apart, placed perpendicular to the side of the fish. Based on this recording the stimulus was appropriately attenuated (PA4; TDT) so as to maintain 5% contrast amplitude modulations (percent of EOD amplitude). Both EOD voltages (head-tail and transverse) were amplified and low-pass filtered at 5 kHz (2015F; Intronix, Bolton, ON, Canada). The extracellular potential, the EOD, the transdermal potential, and the attenuated stimulus were digitized at 20 kHz with a data-acquisition interface (Power 1401; Cambridge Electronics Design, Cambridge, UK) and recorded using Spike2 software (Cambridge Electronics Design). Spike time detection, stimulus generation, and analysis of the data were performed off-line using Spike2 and Matlab software (Mathworks, Natick, MA). Data from 48 single-unit recordings and 5 dual-unit recordings from five adult *A. leptorhynchus* (13–17 cm, 3 males, 2 females) were used.

### Analysis

To determine “synchrony” or “coincidence” between spikes of two P-unit recordings, we centered time windows on the spikes of one of the units. If a spike from the other “comparison” neuron occurred within the window, both spikes were added to the synchronous spike train. When not explicitly mentioned, the synchrony time window was 1 ms wide. The “all spike” trains were simply a linear sum of both P-unit spike trains. From  $n = 48$  single unit recordings there are  $N = n(n - 1)/2 = 1,128$  unique spike train pairs from which we constructed synchronous and summed spike trains.

The coherence function between two time-varying signals is given by:  $C_{sx}(f) = |\langle S_{sx}(f) \rangle|^2 / (\langle S_{ss}(f) \rangle \langle S_{xx}(f) \rangle)$  where  $s(t)$  is the stimulus (0- to 300-Hz Gaussian AM) and  $x(t)$  is the spike train response. The brackets indicate an ensemble average (i.e., a statistical average over repeated trials).  $S_{sx}(f)$  is the cross-spectral power density between  $s(t)$  and  $x(t)$ , and  $S_{ss}(f)$  and  $S_{xx}(f)$  are the auto-spectral power densities of  $s(t)$  and  $x(t)$ , respectively. When numerically calculating the coherence, spike trains were digitized at 1 kHz, giving a sampling cutoff, or Nyquist frequency of 500 Hz (Papoulis and Pillai 2002), and then had their means subtracted. This upper limit is more than sufficient for the 0- to 300-Hz signals used. The coherence between a stimulus and response is related to the lower bound of mutual information between these two signals (Borst and Theunissen 1999; Roddey et al. 2000). To get an estimate of the upper bound of mutual information between stimulus and response, we calculated the square root of the coherence

between two responses to the same stimulus (Roddey et al. 2000). The square root of the response-response coherence is always greater than or equal to the stimulus response coherence, and any difference in the frequency tuning between the two will reveal the presence of nonlinear signal transfer.

The stimulus-response coherences for the postsynaptic neural models were computed in two ways. When CMS models were considered, 16 units were chosen randomly, from the original pool of 48 P-unit recordings, and were used to drive the postsynaptic neural model; this represents a lower bound on the number of P-units that have been anatomically shown to provide a strong input to CMS pyramidal cells (Maler, unpublished observations). This was repeated 20 times, and each time 16 different neurons were chosen randomly. The coherences presented in Fig. 6 are an average of these 20 trial coherences. When the LS model was considered, we created a surrogate for a large population by adding together population activity (sum of all 48 P-unit spike train recordings) from eight different trials, with the same 5-s stimulus presented in all trials. Pyramidal cells of the LS map therefore receive input from 24 times as many P-units as in the CMS map, consistent with anatomical studies (Maler, unpublished observations). The validity of adding multiple realizations together to form a representation of a large population response is based on the fact that P-units have uncorrelated baseline activity (Benda et al. 2006; Chacron et al. 2005).

### Neural models

The current threshold model used in Fig. 6A is a linear rectifier (Rice 1954), the output of which,  $y(t)$ , is given by

$$y(t) = \begin{cases} x(t) - x_{th} & x(t) > x_{th} \\ 0 & \text{otherwise} \end{cases} \quad (1)$$

where  $x(t)$  is the input to the model and  $x_{th}$  is the output threshold. In the  $n = 16$  case, the threshold was set to  $x_{th} = 0$ , which puts the rectifier in the superthreshold regime, effectively acting as a follower of superthreshold inputs. To maintain the same mean output in the  $n = 384$  case, the threshold was set to  $x_{th} = 109$ , which puts the rectifier in the subthreshold regime, acting as a coincidence detector.

We show a similar effect for a spiking, conductance-based neural model of the postsynaptic cell (Fig. 6B). The model used is a modified ghostbuster model (Doiron et al. 2002), a conductance-based, two-compartment (soma and dendrite) neural model with active spike generating currents that was developed to qualitatively describe in vitro data in the ELL. The equations describing our model are

Soma

$$C \frac{dV_S}{dt} = I_S + g_{Na,S} \cdot m_{\infty,S}^2(V_S) \cdot (1 - n_S) \cdot (V_{Na} - V_S) + g_{K,S} \cdot n_S^2 \cdot (V_K - V_S) + \frac{g_C}{\kappa} \cdot (V_D - V_S) + g_{leak} \cdot (V_I - V_S) + g_{K_2} \cdot (V_K - V_S) + g_{syn} \cdot \alpha(t) \cdot (V_{AMPA} - V_S) \quad (2)$$

$$\frac{dn_S}{dt} = \frac{n_{\infty,S}(V_S) - n_S}{\tau_{n,S}} \quad (3)$$

Dendrite

$$C \frac{dV_D}{dt} = g_{Na,D} \cdot m_{\infty,D}^2(V_D) \cdot (1 - n_D) \cdot (V_{Na} - V_D) + g_{K,D} \cdot n_D^2 \cdot (V_K - V_D) + \frac{g_C}{(1 - \kappa)} \cdot (V_S - V_D) + g_{leak} \cdot (V_I - V_D) \quad (4)$$

$$\frac{dn_D}{dt} = \frac{n_{\infty,D}(V_D) - n_D}{\tau_{n,D}} \quad (5)$$

The processes  $V$ ,  $m$ , and  $n$  are membrane voltage, sodium activation, and potassium activation, respectively. The subscripts 'S' and 'D' refer to somatic and dendritic quantities, respectively.  $C$  is the membrane capacitance and  $I_S$  is the mean input bias current to the soma. Maximum conductances for spiking sodium and potassium, soma-dendritic electrical conductance, leak, voltage independent hyperpolarizing potassium and synaptic inputs are represented by  $g_{Na}$ ,  $g_K$ ,  $g_C$ ,  $g_{leak}$ ,  $g_{K_2}$ , and  $g_{syn}$ , respectively. The reversal potentials for sodium, potassium, leak currents and AMPA receptors are  $V_{Na}$ ,  $V_K$ ,  $V_I$ , and  $V_{AMPA}$ , respectively. The sodium activation variable is slaved to the voltage value in both the soma and the dendrite [i.e.,  $m^2 = m_{\infty}^2(V)$ ]. The sodium inactivation is slaved to the potassium activation,  $n$  (i.e.,  $h = 1 - n$ ). Our model differs from the original (Doiron et al. 2002) in that we further reduced it by slaving dendritic sodium inactivation to dendritic potassium activation and removed slow potassium inactivation. It was more recently shown that while pyramidal cells receive broadband input, the depolarizing after potential (DAP) observed at the soma, resulting from dendritic back-propagation, was sufficient to reproduce observed burst activity without the need for a slow dendritic potassium inactivation process (Doiron et al. 2007). We also observed DAPs in our version of the model with an absence of slow inactivating dendritic potassium.

The EPSP input trains,  $\alpha(t)$ , were obtained by convolving experimentally measured spike trains with an alpha function,  $h(t) = \alpha^2 \exp(-\alpha t)$ , with  $\alpha = \sqrt{2}$  kHz, giving a 2-ms EPSP width, reasonable for the observed unitary EPSPs as a result of feedforward activity from the P units in vitro (Berman and Maler 1999; Wang and Maler 1994). The parameter values used were:  $C = 1 \mu\text{F}/\text{cm}^2$ ,  $g_{Na,S} = 55 \text{ mS}/\text{cm}^2$ ,  $g_{K,S} = 20 \text{ mS}/\text{cm}^2$ ,  $g_{Na,D} = 6.5 \text{ mS}/\text{cm}^2$ ,  $g_{K,D} = 10 \text{ mS}/\text{cm}^2$ ,  $g_C = 1$ ,  $g_{leak} = 0.2 \text{ mS}/\text{cm}^2$ ,  $V_{Na} = 40 \text{ mV}$ ,  $V_K = -88 \text{ mV}$ ,  $V_I = -70 \text{ mV}$ , and  $V_{AMPA} = 0 \text{ mV}$ . The activation functions for the conductances had the generic form:  $x_{\infty}(V) = 1/(1 + e^{(V - V_{1/2})/k})$  with  $V_{1/2} = -56 \text{ mV}$  for the dendritic conductances ( $m_{\infty,D}$  and  $n_{\infty,D}$ ) and somatic potassium activation ( $m_{\infty,S}$ ). The parameter,  $k$ , determines the sharpness of the activation curves (i.e., smaller  $k$  gives steeper activation curves). We have used  $k = 3$  and  $5 \text{ mV}$  for the soma and dendrite, respectively. The compartment coupling parameter,  $\kappa$ , was set to 0.4.

Recent studies have shown that, compared with CMS, LS pyramidal cells express high levels of SK channels (Ellis et al. 2007, 2008). Also the spike thresholds of low-frequency-tuned CMS cells and high-frequency-tuned LS cells are  $V_{\text{thresh}} = -67 \text{ mV}$  and  $V_{\text{thresh}} = -62 \text{ mV}$  (Mehaffey et al. 2008), respectively. In light of the differential expression of potassium channels, we gave the CMS and LS neuron different levels of passive potassium conductance:  $g_{K_2} = 0.24 \text{ mS}/\text{cm}^2$  and  $g_{K_2} = 0.5 \text{ mS}/\text{cm}^2$ , respectively. The biophysical basis of the threshold difference is not known, so to obtain appropriate spike thresholds in our models, we followed a suggestion of Mehaffey et al. (2008) and fixed the half max of somatic sodium activation to  $V_{1/2, Na} = -56 \text{ mV}$  for the CMS model and raised it to  $V_{1/2, Na} = -51 \text{ mV}$  for the LS model. This resulted in spike thresholds of  $-65$  and  $-59 \text{ mV}$ , respectively. The spike threshold criterion was based on the first derivative of the voltage: the threshold was the observed voltage when the derivative of the voltage was eight times greater than the SD of the derivative of the subthreshold voltage fluctuations. The final difference between the two models was the synaptic conductance:  $g_{syn} = 0.027 \text{ mS}/\text{cm}^2$  and  $g_{syn} = 0.005 \text{ mS}/\text{cm}^2$  for CMS and LS, respectively. Although the parameters  $g_{K_2}$  and  $g_{syn}$  were not quantitatively based on experimentally observed values, they were both adjusted to limit the output firing rate of the models once the spike thresholds were set to measured values (Mehaffey et al. 2008). For the values of  $g_{K_2}$  and  $g_{syn}$  chosen, the coefficient of variation (CV) of the interspike intervals (ISIs) was 1.03, within the range observed for E-type pyramidal cells in LS,  $1.19 \pm 0.31$  (Krahe et al. 2008). If  $g_{K_2}$  and  $g_{syn}$  are held at the CMS values ( $0.24 \text{ mS}/\text{cm}^2$  and  $g_{syn} = 0.027 \text{ mS}/\text{cm}^2$ , respectively) and only the spike threshold is increased to maintain a firing rate of  $\sim 30 \text{ Hz}$ , the CV increases to 2.14, inconsistent with observed values.

The synaptic conductance in the LS model was reduced with respect to the CMS model to maintain physiological levels of membrane fluctuations in the face of an order of magnitude increase in the number of inputs. Whether or not there are differences in the unitary synaptic conductances between ELL maps remains to be verified.

In both models, the output rate (i.e., mean level of superthreshold current for the threshold model and mean spike rate for the ELL pyramidal cell model) was normalized to the same fixed value for both CMS models and LS models by adjusting intrinsic parameters as described in the preceding text. These parameter changes were motivated by *in vitro* ELL data (Ellis et al. 2007, 2008; Mehaffey et al. 2008) for the spiking ELL pyramidal cell model. This normalization ensured covariation of RF size and frequency tuning.

## RESULTS

### Encoding of broadband EOD amplitude modulations by synchronous and asynchronous P-unit spikes

The baseline discharge of P-units is uncorrelated (Benda et al. 2006; Chacron et al. 2005), but they synchronize specifically to the high-frequency, sinusoidal AMs that occur in the context of social aggregation (Benda et al. 2006). They also partially synchronize when given broadband (0–300 Hz) Gaussian random amplitude modulations (RAMs; Fig. 1). P-units are anatomically uncoupled, and their synchronous spike discharge occurs reliably around certain times with respect to the RAM (Fig. 1), thus their synchronous activity is stimulus driven. We propose that the frequency content of the broadband stimulus that is encoded by postsynaptic cells will depend on the amount of afferent convergence they receive. Each P-unit afferent trifurcates to innervate pyramidal cells in all three ELL maps (Carr et al. 1982; Heiligenberg and Dye 1982). However, the ratios of convergence (i.e., number of afferents synapsing onto a single pyramidal cell) are different across the maps with convergence ratios in the LS being higher

than in the CMS (Maler, unpublished observations). As a result, a cell with a small RF receiving little convergent input has a summed synaptic conductance with a small mean and variance (illustrated in Fig. 2A). A cell with a large RF, with greater afferent convergence, experiences a total synaptic conductance with higher mean and variance.

Despite these likely differences in afferent synaptic drive, pyramidal cell firing rates in the different ELL maps are roughly conserved (Krahe et al. 2008), implying a mechanism to maintain a fixed output rate. Tuning the input-output threshold offers a simple means of maintaining output rate and appropriate intrinsic threshold differences have already been reported between CMS and LS pyramidal cells (Mehaffey et al. 2008). A higher threshold relative to the mean glutamatergic depolarization in an LS cell will allow only large excursions of synaptic conductance to initiate spiking output and, if tuned properly, maintain the same output discharge rate as in the case of a cell receiving less convergent input. This effect can be captured with a simple threshold mechanism (Fig. 2B).

To assess the stimulus characteristics selected by synchronous population activity and passed to a high-threshold decoding postsynaptic unit, the total stimulus information carried by pairwise synchronous activity must first be quantified. Spikes from recorded P-unit spike trains were considered “synchronous” if they occurred within a small time window (1-ms width) centered on any spike of a second spike train (Fig. 3A). “Synchronous spike trains” consisting of spikes from both P-units chosen based on this criterion were further compared with “all spike trains” consisting of a summation of spikes from both P-units (Fig. 3A).

The coherence function quantifies the correlation between two time-varying signals as a function of their frequency components (Papoulis and Pillai 2002). When applied to all experimentally measured spikes of paired P-unit activity, the coherence of this spike train with the sensory stimulation (the 0- to 300-Hz RAM) is broadband with a peak of ~27 Hz (Fig. 3B, dashed line,  $n = 48$  single units,  $n = 1,128$  pairs). The coherence eventually decays down to zero for extremely high frequencies (>200 Hz). Because of the very slow rate of linear decay of the coherence we label it “broadband.” The broadband “all spike coherence” is expected given observed P-unit broadband single-cell properties (Chacron et al. 2005). In contrast, the “synchronous spike” coherence is high-pass, peaking at a much higher frequency (~100 Hz, Fig. 3B). The fluctuations in the trial-averaged coherence curves cannot be averaged out because the same 4-s frozen noise stimulus was used across all response trials to allow for calculations of stimulus-induced synchrony. It is important to note that the effect we are focusing on is not a computation that maximizes information, but rather one that performs frequency-dependent filtering. Namely, synchronous spikes encode more information about high-frequency stimulus components than they do about low-frequency components but *not* more information about high-frequency stimulus components than the corresponding summed spike train. By necessity, the synchronous spike trains will have less information than summed spikes by the data processing inequality (Borst and Theunissen 1999) as they are derived from the summed spike train by deleting spikes.

To confirm the validity of pair-wise comparison of single-unit recordings, we obtained a limited number of dual unit

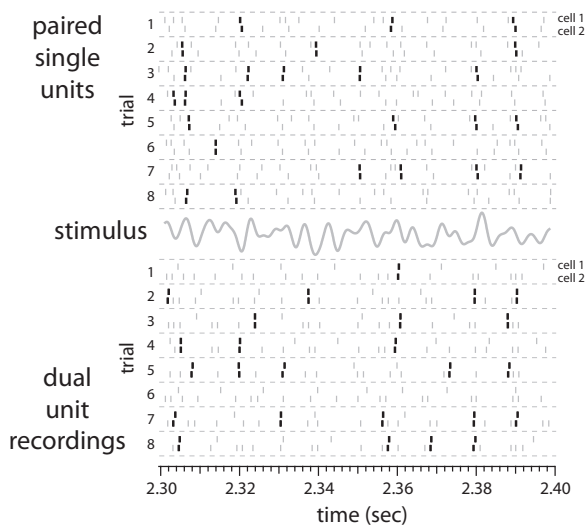


FIG. 1. P-unit spikes synchronize reliably in response to broadband electric organ discharge (EOD) amplitude modulations. A raster plot of 8 trials of a pair of nonsimultaneously recorded single P-units shows the reliable spikes (occurring within a 1-ms time window) in thick black ticks (*top*). An example dual unit (simultaneous) recording directly shows synchronization (*bottom*). Both examples are in response to the same 0- to 300-Hz Gaussian random AM of the electric organ discharge (*middle*). The reliable firing of synchronous spikes at similar times with respect to the stimulus waveform in different single units or dual-unit recordings shows that the synchrony is stimulus driven.

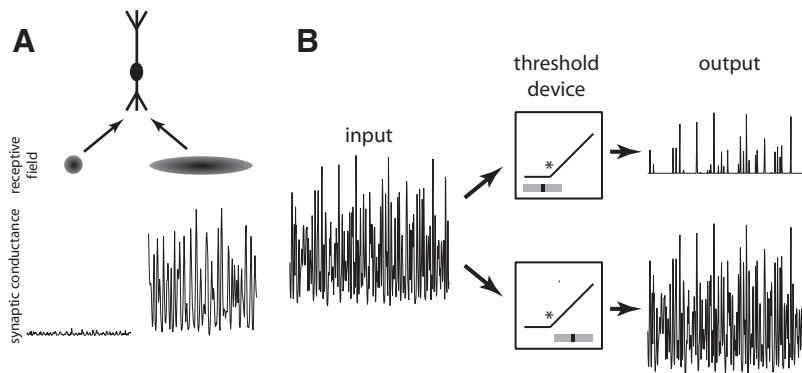


FIG. 2. Receptive field (RF) size of a pyramidal cell will depend on the amount of afferent convergence and determines postsynaptic conductance. *A*: a small RF will result in a time-dependent conductance with smaller mean and variance (*left*). A large RF will result in a conductance with larger mean and variance (*right*). *B*: synaptic conductance with large mean and variance is input into a linear rectifier. If the mean of the input (■) is below threshold only some of the input is transferred, resulting in an output with a reduced mean value (*top*). If the entire range (⊞) of the input is above threshold the output is identical to the input (*bottom*). \*, the rectifying threshold.

recordings (Fig. 3C;  $n = 5$  dual-unit recordings). Synchronous spikes from simultaneous recordings perform the same high-pass computation as pairs of separate recordings. This is expected because P-unit activity exhibits no baseline (noise) correlations (Benda et al. 2006; Chacron et al. 2005). By randomly shuffling the order of trials in the dual-unit recordings, we see the same high-pass computation by synchronous spikes (Fig. 3D), again corroborating what we expected due to the lack of noise correlations.

To examine whether or not there are significant nonlinearities in the transfer of information by synchronous spikes, we calculated the square root response-response coherence (Borst and Theunissen 1999; Roddey et al. 2000). Figure 3E shows the stimulus response coherences between the stimulus and either the synchronous or summed spike

trains (thick curves), as well as the coherence between different trials of either the synchronous spike responses or the summed spike responses. As expected, the square root response is larger but still maintains the same frequency dependence in its tuning. Because of the lack of qualitative discrepancy between linear and nonlinear information transfer, we will continue to use stimulus response coherence for the remainder of the analysis.

#### Selective extraction of synchronous spikes by neurons with large RFs

Inputs to neural models were derived from the P-unit data by convolving recorded spike trains with 2-ms-wide alpha functions (see METHODS), giving EPSP trains that resemble the fast

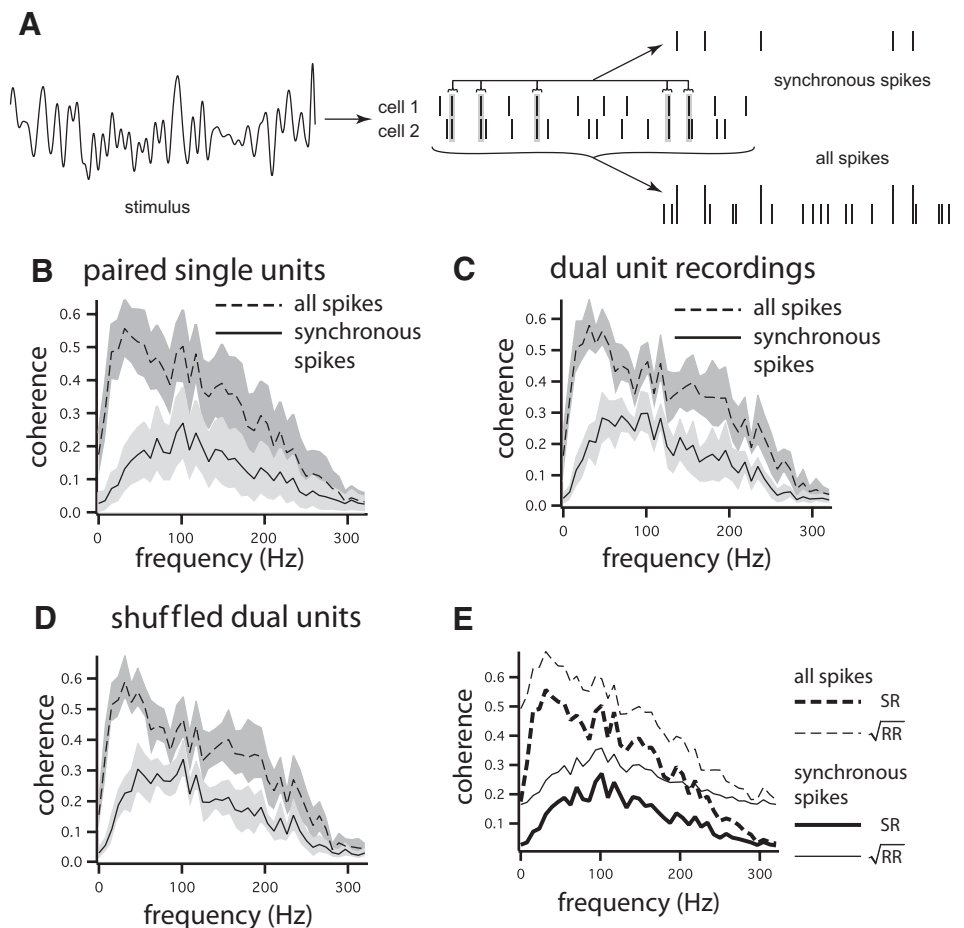


FIG. 3. Synchronous spikes preferentially encode high-frequency sensory information. *A*: a 0- to 300-Hz Gaussian-distributed AM (*left*) drives different P units, labeled “cell 1” and “cell 2”. The spike trains are digitized at a 1-kHz sampling rate. Spikes occurring in the same 1-ms time bin (gray box) are considered synchronous. The surrogate spike trains under consideration are the synchronous spike train (*top right*) and the summed spike train (*bottom right*). *B*: the average coherence between 0- and 300-Hz random AM electrosensory stimuli and synchronous spike trains of pairs of P units (solid line) or summed spike trains of P-unit pairs (dashed line;  $n = 48$  single units,  $n = 1,128$  pairs). Shaded areas indicate the  $\pm 1$  SD. *C* and *D*: the average coherence of synchronous (solid line) and summed (dashed line) spike trains from dual unit recordings and from shuffled trials in dual-unit recordings ( $n = 5$  pairs), respectively. *E*: the stimulus-response coherences (SR, thick lines) between the broadband stimulus and either synchronous spikes (solid line) or summed spike trains (dashed line). The square root of the response-response coherence ( $\sqrt{RR}$ , thin lines) between different trials of synchronous spikes (solid line) and summed spikes (dashed line) is higher than but qualitatively the same as the corresponding stimulus-response coherence curves.

excitatory component of P-unit EPSPs on pyramidal cells (Berman and Maler 1998). The single events comprising EPSP trains, resulting from this form of convolution, have comparable rise and decay times. Even though rise and decay times of observed EPSPs differ slightly (Berman and Maler 1998), we used this simple model of EPSP waveform to focus only on the effects of EPSP width. RF size was implicitly controlled in the model by changing the afferent population sizes. A small afferent population contained data from  $n = 16$  P-units, whereas a large afferent population contained data from  $n = 384$  P-unit recordings (constructed from 8 independent realizations of the responses from 48 different P-units). The convergence ratios, 16:1 (CMS) and 384:1 (LS), are on the same order as observed convergence ratios of the ELL maps:  $\sim 25:1$  (CMS) and 600:1 (LS) (LM, unpublished observations).

The type of output from a postsynaptic receiver will depend on the temporal relationship of its incoming presynaptic spikes. Synchronous presynaptic spikes will still elicit postsynaptic output even when the postsynaptic current threshold is high, whereas isolated spikes will not (Fig. 4A). A lower threshold will allow both isolated and synchronous presynaptic spikes to impact the postsynaptic output (Fig. 4B).

A simple neural model based on detection and transmission of superthreshold current inputs (see METHODS) will reproduce the broadband/high-pass information transmission dichotomy seen in the analysis of paired recordings with the control of a single, intrinsic parameter: the current threshold. When this current threshold model is in receipt of the small afferent input population, the threshold is set low so that all inputs are transmitted. In this case, the coherence between the peripheral sensory information driving the afferents (0- to 300-Hz Gaussian noise amplitude modulations) and the neural output is broadband (Fig. 4C, dashed line). When this neural model is in receipt of the large afferent population input, the threshold is raised to maintain the same average output level (average of the current above threshold; see METHODS: neural models). With this form of output normalization the coherence becomes high-pass (Fig. 4C, solid line).

Because the current threshold model is a highly simplified neural model, it lacks in biophysical realism. The minimal number of model parameters allowed us to isolate the responsible mechanism for the transmission of information carried by synchronized spikes. In the following, we show that a more realistic model will exhibit qualitatively the same behavior as the current threshold model, provided its spike threshold is varied in an analogous manner. The more realistic model was a conductance-based, compartmental model of ELL pyramidal cells (Doiron et al. 2002) previously developed to describe bursts generated in ELL pyramidal cells, *in vitro*. There are several mechanisms that could potentially differentiate the ability of ELL segments to detect coincident inputs. Some of these include a dynamic threshold (Azouz and Gray 2000) or synaptic depression (de la Rocha and Parga 2005; Senn et al. 1998); there is, however, no evidence for differences between LS and CMS with respect to these putative mechanisms. However, a recent *in vitro* study has demonstrated different spike thresholds between low-frequency-tuned CMS cells ( $V_{\text{thresh}} = -66.99$  mV) and high-frequency-tuned LS cells ( $V_{\text{thresh}} = -61.73$  mV) (Mehaffey et al. 2008); because these results were obtained with intracellular current injection, they demonstrate that this threshold difference is intrinsic to pyramidal cells. In addition, a recent study has also shown high levels of expression of SK channels and SK-mediated afterhyperpolarizations (AHPs) in LS pyramidal cells; in contrast SK mRNA and medium AHPs are lacking in most CMS pyramidal cells (Ellis et al. 2007, 2008). This extra hyperpolarizing potassium current in LS pyramidal cells will reduce the average voltage with respect to threshold.

To incorporate these differences, we increased the hyperpolarizing potassium conductance,  $g_{K2}$ , and shifted the somatic sodium activation curves to more depolarized values (to mimic the physiological data) for the LS model (see METHODS). It is likely that GABA<sub>A</sub>-mediated hyperpolarizing inhibition is also more prominent in LS compared with CMS and contributes to greater gain control in LS (Maler and Mugnaini 1994; Mehaffey et al. 2005; Shumway and Maler

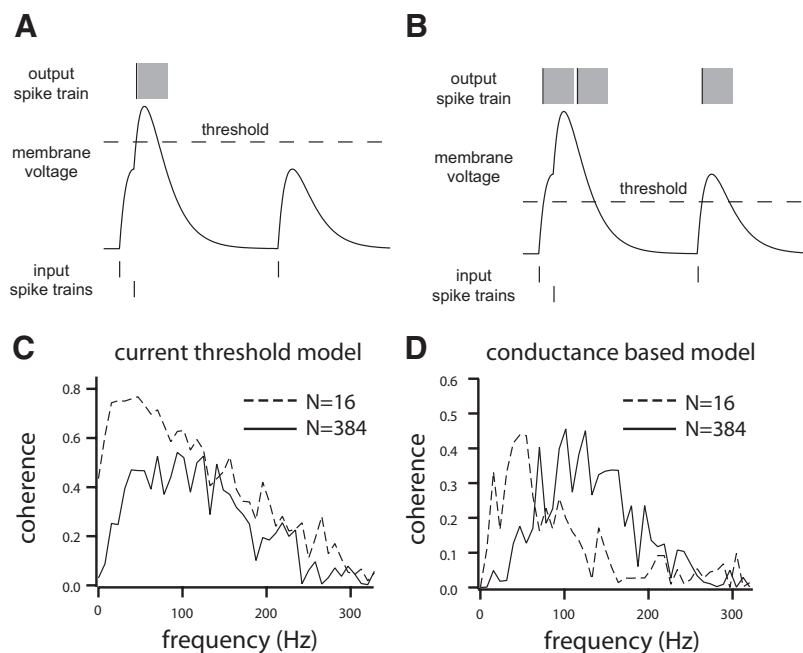


FIG. 4. Decoding high-frequency information from synchronous afferent spikes. *A*: presynaptic spike trains (*bottom*) give rise to postsynaptic potential (PSP) trains (*middle*) in a simplified threshold-based neural model. When the spiking threshold (dashed line) is higher, only synchronous spikes will evoke a response spike. The shaded regions indicate, the relative refractory period of the postsynaptic spike generation mechanism. *B*: when the spiking threshold is lower, isolated spikes will evoke a postsynaptic spike, whereas synchronous spikes will evoke one or more postsynaptic spikes. *C*: the coherence between the electrosensory stimulus and the output of the current threshold model receiving different numbers of summed EPSP trains from P-unit data ( $n = 16$ , dashed line;  $n = 384$ , solid line). The threshold has a value of 0 for the  $n = 16$  case, and a value of 109 for the  $n = 384$  case, such that the averaged output in both cases is the same. *D*: the coherence between the electrosensory stimulus and the output of a conductance-based, compartmental pyramidal cell model receiving different numbers of summed excitatory postsynaptic current (EPSC) trains from P-unit data ( $n = 16$ , dashed line;  $n = 384$ , solid line). The segment specific parameters used are  $g_{K2} = 0.24$  mS/cm<sup>2</sup>,  $V_{1/2, Na} = -56$  mV, and  $g_{syn} = 0.027$  for the centromedial segment (CMS) model and  $g_{K2} = 0.5$  mS/cm<sup>2</sup>,  $V_{1/2, Na} = -51$  mV, and  $g_{syn} = 0.005$  for the lateral segment (LS) model. See METHODS for a list of remaining parameters. These parameter were all chosen to maintain the same output firing rate (30 Hz).

1989); we did not explicitly model this circuitry but consider the potential difference between CMS and LS to be qualitatively described by the greater hyperpolarization current in LS model neurons.

The CMS model cell (i.e., less hyperpolarizing potassium current and low spike threshold) spike train coherence is low-pass with respect to the sensory input, as expected (Fig. 4D, dashed line), as is in fact observed for CMS pyramidal cells in vivo (Krahe et al. 2008; Shumway 1989) and in vitro (Mehaffey et al. 2008). LS units receive a far greater number of inputs as a result of their larger RFs. The level of hyperpolarizing potassium conductance and sodium activation threshold in our model was tuned to limit the output firing rate to that of the CMS model neuron ( $\sim 30$  Hz). In this case, the stimulus-response coherence of the LS model is high-pass (Fig. 4D, solid line), as expected from recent in vivo data (Krahe et al. 2008). In the current threshold model, the coherence of the CMS model is larger than that of the LS model for all frequencies. The coherence of the conductance-based LS model is higher than that of the corresponding CMS model at higher frequencies ( $>100$  Hz); even though the qualitative filtering properties are invariant for both sets of models (i.e., CMS is low-pass, LS is high-pass), the difference in relative coherences occurs because there is no integration time constant in the current threshold models while the high-conductance state of the LS conductance-based model likely decreases its time constant and allows it to track high frequencies (Destexhe et al. 2003).

It should be noted that the coherences for both current threshold models are larger than both coherences for the conductance-based models. This can be understood in the context of the data processing inequality, which states that any nonlinear transformation of a signal reduces the amount of information contained in that signal. The current threshold model involves only one transformation: a thresholding of the input, resulting in an analog signal. The conductance-based model involves subthreshold nonlinearities plus a nonlinear “analog-to-digital” spike generation transformation. Hence it is expected that the conductance-based model reduces the information carried in the output more than the

current threshold model does. As well, the subthreshold temporal filtering in the conductance-based model causes the high-frequency components of its respective coherences to drop off faster than those of the current threshold model, which has no dynamics.

Recently a cross-map comparison of coherences between RAMs and ELL pyramidal cell spike trains was performed experimentally (Krahe et al. 2008). We cannot quantitatively compare our model results with these data because we used RAMs of 0–300 Hz (to match the maximal stimulus range expected in this species), whereas Krahe et al. (2008) used RAMs of 0–120 Hz. However, as might be expected, the conductance-based model is clearly a better qualitative match to the experimental data of Krahe et al. (2008) than the simple threshold model. This can readily be appreciated from the fact that, in the conductance-based model of the CMS pyramidal cell (but not the threshold model), the coherence drops off very rapidly with frequency [compare our Fig. 4, C and D, with Krahe et al. (2008), Fig. 3A]. Both the approach of Krahe et al. (2008) and the one taken in this study reveal information about different aspects of the transfer of electrosensory signal from periphery to pyramidal cells. Our modeling-based approach enabled us to assess the biophysical ingredients that underlie the qualitatively similar features of the input-pyramidal cell coherence found in both approaches.

To isolate the effect of the spike threshold, the sodium activation curve of the LS model was shifted from  $V_{1/2, Na} = -51$  mV to more hyperpolarized values ( $V_{1/2, Na} = -56$  mV), the same as in the CMS model, without modifying other parameters. This activation shift lowered the mean threshold from  $-59$  to  $-65$  mV (Fig. 5A). As expected, from the current threshold model, the spike coherence became broadband (Fig. 5B), as is the case for the CMS model with the same low spike threshold ( $-65$  mV). However, the resulting firing rate of the LS model with the decreased spike threshold increased to a much higher and unphysiological value of 253 Hz. As an additional test of the role of spike threshold in high-pass filtering, we tested the effects of the other parameters used to control output firing in the LS model,  $g_{K2}$  and  $g_{syn}$ . When the

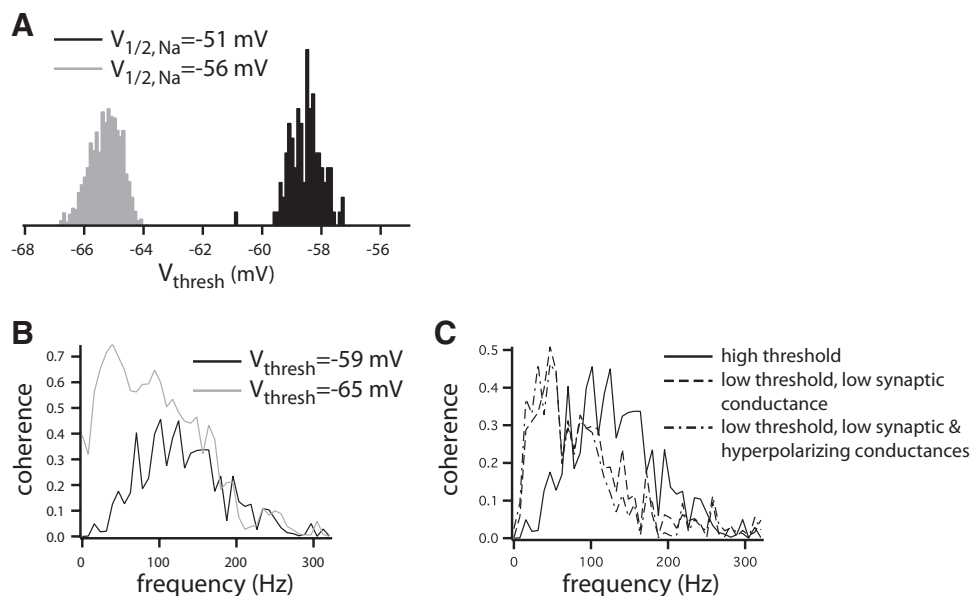


FIG. 5. The effect of spike threshold on postsynaptic decoding. *A*: when the half-maximum of the somatic sodium activation is lowered from  $V_{1/2, Na} = -51$  mV to  $V_{1/2, Na} = -56$  mV, the voltage threshold decreases from  $-59 \pm 2.0$  mV (black) to  $-65 \pm 1$  mV (grey). *B*: with a high threshold and high levels of convergent input, the spike train coherence of the pyramidal cell model is high-pass (black). When the spike threshold is lowered compared with observed values in high-frequency-tuned LS cells (Mehaffey et al. 2008), the coherence becomes broadband (grey); however, the mean firing rate is also increased to 253 Hz. *C*: when the spike threshold is lowered to CMS values ( $-65$  mV) and the synaptic scaling is reduced ( $g_{syn} = 0.0011$  mS/cm<sup>2</sup>) to maintain output firing rate at CMS values ( $\sim 30$  Hz), the coherence becomes low-pass. When  $g_{K2}$  is reduced to CMS levels (0.24 mS/cm<sup>2</sup>) and the synaptic scaling is reduced even further ( $g_{syn} = 0.0009$  mS/cm<sup>2</sup>) to maintain firing rate, the coherence is still low-pass.

threshold was reduced to CMS values ( $-65$  mV), the synaptic conductance,  $g_{\text{syn}}$ , was additionally reduced to  $0.0011$  mS/cm<sup>2</sup> to maintain the same firing rate as the CMS model ( $\sim 30$  Hz). This still results in low-pass coherence relative to the LS model (Fig. 5C, dashed line). When the hyperpolarizing conductance,  $g_{\text{K2}}$ , was reduced to that of the CMS model ( $0.24$  mS/cm<sup>2</sup>), the synaptic conductance had to be further reduced ( $g_{\text{syn}} = 0.0009$  mS/cm<sup>2</sup>) to again maintain the same firing rate. In this case, the coherence between the stimulus and the output spike train is also low-pass (dash-dot line). These simulation results suggest that the role of these other parameters is to maintain physiological firing rates, whereas the physiologically observed variation in spike threshold across sensory maps is the most relevant parameter in determining the selective extraction of high-frequency information from synchronous spikes.

The qualitative agreement between the coherence of synchronous presynaptic spikes and the coherence of a high-threshold postsynaptic cell is compelling evidence for the role of afferent convergence and postsynaptic spike threshold in matching the frequency selectivity of synchronous spike and postsynaptic response. We directly compared the timing of pairwise synchronous presynaptic spikes and the superthreshold current from the current threshold model in the high convergence scenario. Figure 6 shows the output of the simple current threshold model when it is tuned to the large afferent input population (solid line). The scaled histogram of synchronous spike times from the pairwise P-unit analysis, with a 2-ms coincidence window (grey line), reveals a tight correspondence between the timing of pairwise synchronous events and postsynaptic response. It can also be seen here that the temporal precision is increased when one considers superthreshold population response over pairwise synchronous events.

#### Effects of synaptic timescale on transmission of information by synchronous spikes

In the ELL, the width of EPSPs is controlled by GABA<sub>A</sub>-mediated inhibition (Berman and Maler 1998). EPSPs evoked by electrosensory afferents peak at 1–2 ms and decay with a time scale of 10 ms. The superimposed GABA<sub>A</sub> inhibitory postsynaptic potentials (IPSPs) peak at 4–6 ms resulting in a mixed PSP (net excitatory) with a width of  $\sim 2$  ms. Because of this tightly regulated compound PSP width, the effect of synaptic time scale should impact signal transmission through the postsynaptic unit. Increasing EPSP width,  $\Delta t$ , reduces the

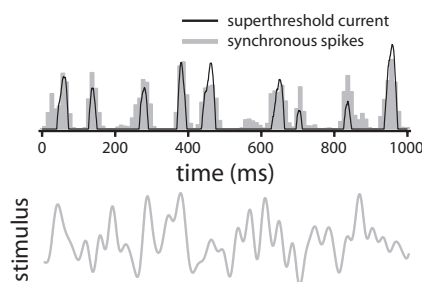


FIG. 6. Superthreshold population current arises, in large part, from pairwise synchronous events (*top*). For short synchrony time windows ( $\Delta t = 2$  ms shown), the synchronous spike time histogram corresponds to the superthreshold current of a large afferent population with the same excitatory postsynaptic potential (EPSP) width ( $\Delta t = 2$  ms,  $n = 384$  and  $x_{\text{th}} = 109$  of the current threshold model). *Bottom*: corresponding amplitude modulation (AM).

effect of presynaptic spike time precision on the postsynaptic conductance. This width increase, along with the appropriate output rate normalization in the current threshold model, results in increased coherence in the low-frequency range (10–40 Hz; Fig. 7A). This is accompanied by a decreased coherence in a high-frequency range (110–140 Hz; Fig. 7A). Figure 7B shows examples of the full frequency-dependent coherences for a range of EPSP widths between 1 and 9 ms. It is therefore possible that the more potent GABAergic inhibition in LS (Maler and Mugnaini 1994) shortens EPSP duration in that segment so as to maintain the high-frequency tuning conferred by the combination of the large RFS of its neurons and their higher threshold and greater SK channel density.

Decoding broadband inputs with synchronous spikes from pairs of P-units results in a high-pass filtering computation (Fig. 3). Properly tuned decoders receiving inputs from a large population of P-units perform the same qualitative computation (Figs. 4 and 5). But are the threshold-crossing events of a large P-unit population composed of pairwise synchronous events? This depends on the size of time window for categorizing these events. As the window size,  $\Delta t$ , increases, a larger fraction of all spikes,  $N_{\text{all}}$ , will additionally be counted as synchronous spike,  $N_{\text{synch}}$  (Fig. 8A). As the criterion for coincidence relaxes, the synchronous spike train becomes more coherent with low frequencies (Fig. 8B). The same low-frequency coding is observed in CMS model neurons receiving small afferent populations (Fig. 4) or an LS model neuron in receipt of a large population of afferent inputs that are low-pass filtered by EPSPs with large time constants (Fig. 7).

#### Response latency and frequency tuning properties

To establish a connection between short-latency response and high-frequency tuning of the LS compared with the CMS maps, the conductance-based models were given simulated Poisson spike train inputs the firing rates of which were increased in an instantaneous, step-like manner and latencies were quantified (Fig. 9). Note that the synaptic input was implemented as instantaneous changes in conductance and so did not consider the synaptic and conduction delays from P units to pyramidal cells (Bastian 1981). The CMS model received 16 Poisson spike train inputs while the LS model received 384 Poisson inputs with individual firing rates of 197 Hz, the average firing rate observed in recorded P-unit activity. For a given rate of presynaptic input, the postsynaptic firing rate will depend on the correlation between inputs (Salinas and Sejnowski 2000). The correlation coefficient of the Poisson inputs was adjusted to  $\sim 0.2$  so that the firing rates of the CMS and LS models matched their rates when they received real P-unit inputs. This was higher than the observed average correlation coefficient (0.124) between recorded P-unit spike trains, but this discrepancy may be due to differences in temporal spike patterns between Poisson processes and physiological P-unit spike trains. When the instantaneous firing rate is increased by 20% (at an arbitrary time of 0 ms), the peristimulus time histogram (PSTH) of the LS model increases very rapidly and peaks at  $\sim 0.6$  ms (Fig. 9A, grey bars) while the PSTH of the CMS model rises more slowly and peaks around 3 ms (Fig. 9A, black bars). Figure 9B shows the probability densities,  $p(t)$ , of the latency to first spike (grey bars) after the step increase for the LS (*left*) and CMS (*right*) models. In the absence of an input step increase, both models would fire after an arbitrary reference time

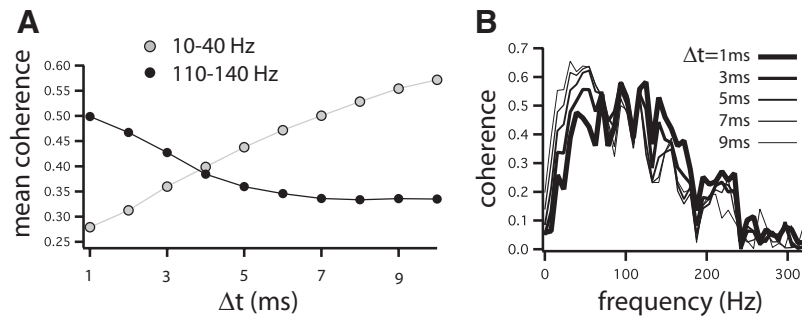


FIG. 7. The effect of synaptic time scale on frequency tuning of a postsynaptic model with a fixed output level (firing rate or mean output of linear rectifier). The current threshold model shown in Fig. 5A is used here. *A*: the coherence, averaged over a low-frequency interval (10–40 Hz), increases with increasing EPSP width,  $\Delta t$  (open symbols). The coherence, averaged over a high-frequency interval (110–140 Hz), decreases with increasing EPSP width (filled symbols). As EPSP width was changed, the threshold of the current threshold model was adjusted to maintain a constant output level. *B* Examples of the full coherence profiles for a range of EPSP widths from 1 ms to 9 ms (thick to thin lines).

because they are spontaneously active. To disambiguate spontaneous activity from step-induced activity, we calculated the latency to first spike in the absence of a step increase (with respect to an arbitrary reference time), as a control (black bars). The control probability densities were then subtracted from the latency to first spike probability densities to show the increase in probability above chance,  $\Delta p(t)$ , of firing after a step increase in input Poisson firing rates (Fig. 9C). The LS is most likely to fire (above chance) 0.3–0.9 ms after the input step increase, whereas the CMS model is most likely to fire 2–10 ms afterward. This confirms that the biophysical and anatomical properties, high spike threshold and high synaptic convergence, that confer the ability of LS pyramidal cells to preferentially encode high-frequency inputs also allow these cells to respond to rapid increases of signal amplitude with very short latencies.

#### DISCUSSION

Pyramidal cells in each map of the ELL have different sized RFs. The LS has pyramidal cells with large RFs (Shumway 1989) and convergence ratios ( $\sim 600:1$ , unpublished observation); LS pyramidal cells are sensitive to high-frequency signals including fast transients (Krahe et al. 2008; Shumway 1989). The CMS has smaller RFs and thus smaller convergence ratios ( $\sim 25:1$ , unpublished observation). It is tuned to lower frequencies (Krahe et al. 2008) and is involved in the jamming avoidance response (Metzner and Juranek 1997) (a behavior associated with low-frequency signals).

We have shown through computational analysis how the extent of afferent convergence (RF size), together with an output rate control, regulates the extraction of synchronous synaptic input: neurons with large RFs and a high relative threshold will selectively respond to synchronous input. The pyramidal cell model parameters for convergence, expression of hyperpolarizing currents and spike thresholds were based on experimentally estimated values for two brain stem electrosensory maps (CMS-minimal convergence, low levels of hyper-

polarization and low spike threshold; LS-maximal convergence and strong hyperpolarization and high spike thresholds). Further, we have experimentally demonstrated that, in response to stimulation with broadband naturalistic signals, synchronous discharge of electrosensory afferents (P-units) preferentially encodes the high-frequency components associated with communication signals. The mechanism that allows P-units to synchronize is not fully understood and requires further modeling studies. When a population of P-units was used to drive the CMS and LS model neurons, we found parallel processing of low (CMS)- and high-frequency (LS) signal components. The high-frequency tuning in LS also required short-duration input EPSPs. Short EPSP durations have been observed in this (Berman and Maler 1998) and other systems (Cruikshank et al. 2007; Wehr and Zador 2003). This result is consistent with experimental studies that have demonstrated that CMS is selective for low-frequency input, whereas LS responds to high-frequency signals (Krahe et al. 2008; Shumway 1989).

Remarkably this association of RF size and fast or high-frequency signals is also seen in the mammalian visual system from retina to LGN to cortex (Malone et al. 2007; Wässle 2004; Weng et al. 2005). Therefore the evolutionary advantage of having two-dimensional (2D) RFs of different sizes may be to tune sensory neurons to different frequency ranges. In the somatosensory system, large 2D RFs are better than small RFs at discriminating stimulus position based on a spike latency code (Foffani et al. 2008). It will be of interest to see whether the ability of somatosensory neurons to track fine temporal stimulus features will depend on RF size as they do in the electrosensory system.

It should be noted that this form of parallel processing is different from the one shown in a study of parallel processing of narrowband signals in the ELL (Middleton et al. 2006). In that study, it was determined that nonlinear features of a narrowband signal were being processed separately from the narrowband signal itself, by different cell types in the same

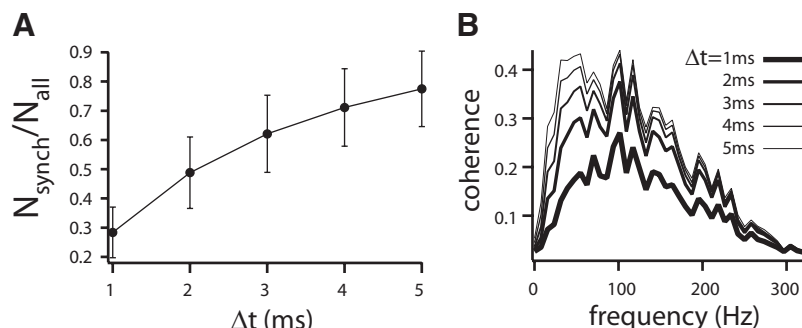
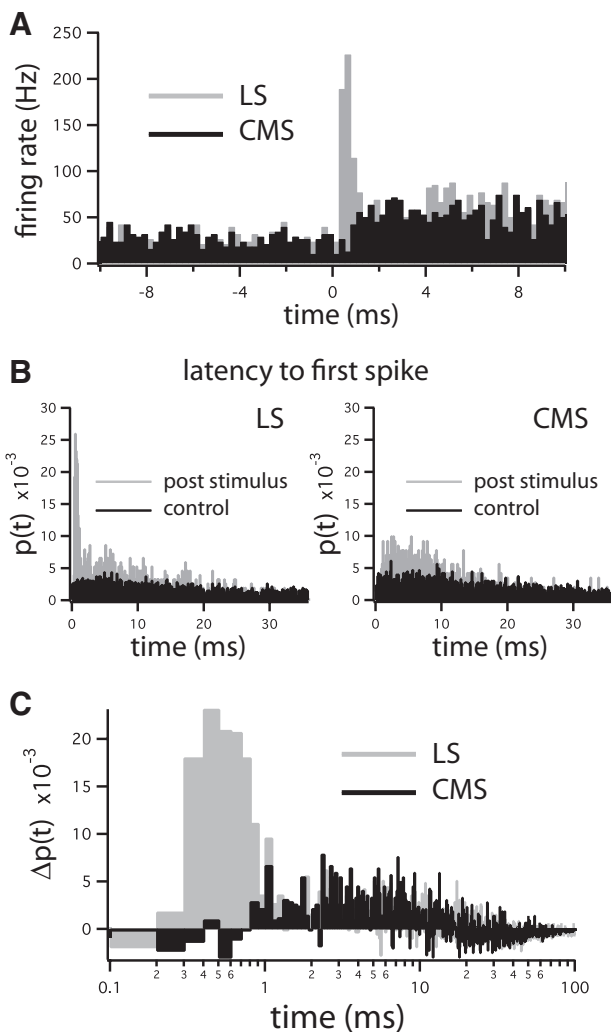


FIG. 8. The effect of synchronous spike time criteria on the frequency tuning of pairwise synchronous spike responses. *A*: the average fraction of synchronous spikes,  $N_{\text{synch}}$ , to all spikes,  $N_{\text{all}}$ , between a pair of P units increases with the width of the synchrony window,  $\Delta t$ . *B*: as the width of the synchrony window increases, the coherence increasingly resembles that for all spikes.



**FIG. 9.** A high-frequency-tuned neural model responds to step conductance increases with shorter latencies than a low-frequency-tuned model. **A:** the peristimulus time histogram (PSTH) of the LS model increases rapidly immediately after the time of conductance increase (0 ms), peaking at  $\sim 0.6$  ms (grey bars). The PSTH of the low-frequency-tuned CMS model, receiving less convergent input, rises more slowly with a less pronounced peak at  $\sim 3$  ms. **B:** the probability density,  $p(t)$ , for latency to 1st spike for the LS model (grey bars, *left*) shows a narrow peak at small times, whereas that of the CMS model (grey bars, *right*) is broader and centered at larger times. Black bars, the control probability densities for latency to 1st spike in the absence of a step conductance increase. **C:** the increase in the probability latency to 1st spike,  $\Delta p(t)$  (i.e., the probability density in the presence of a step minus the probability density in the absence of a step), is peaked at very early times ( $\sim 0.3$ – $0.9$  ms) for the LS model (grey bars) and later ( $\sim 2$ – $10$  ms) for the CMS model.

ELL segment, whereas the current study shows a putative parallel processing of different bandwidths of the same signal by cells in different sensory maps. This latter form of processing emphasizes the role of synchronously firing afferents. Additionally, an *in vitro* study of ELL pyramidal cells showed that information “channels” with different frequency selectivities can be derived from the spike train of a single neuron by selecting either high-frequency spike events or isolated spikes (Oswald et al. 2004).

Large RFs and output rate normalization places cells in the subthreshold, or fluctuation-driven regime. In this regime, the postsynaptic neuron is highly influenced by input fluctuations rather than by the mean bias of the inputs (Softky and Koch

1993), and the largest fluctuations are caused by synchronous spikes. It is also known that positive correlations between neurons increase the variability of their pooled response (Salinas and Sejnowski 2000). Because the large RF neurons encode high-frequency communication signals (Ellis et al. 2007, 2008; Krahe et al. 2008; Mehaffey et al. 2008; Shumway 1989), this result has behavioral relevance. As we have shown, large RF cells with threshold-controlled output rates are sensitive to synchronous inputs and are therefore well suited to further transmit this high-frequency information. The mechanism we describe is consistent with previous observations that stimuli with a large spatial extent result in high-pass coherence in LS pyramidal cells (Chacron et al. 2003). This type of processing was thought to occur through nonlinear integration of synaptic inputs with large spatial extent (Chacron 2006; Krahe et al. 2008). This is consistent with our results showing that postsynaptic coincidence detection (a nonlinear computation) gives high-pass coherence, whereas postsynaptic summation (a linear computation) gives low-pass coherence.

More generally we conclude that the combination of a sensory neuron’s RF size, gain, threshold, and EPSP duration will determine its sensitivity to features selectively encoded by synchronous versus asynchronous input. There is abundant evidence for the importance of synchronous spiking activity in neural computations as well as for the dynamic regulation of relative threshold. In the visual system, synchronous spikes have been shown to improve stimulus reconstruction in the retina (Dan et al. 1998), efficiently drive thalamocortical pathways (Bruno and Sakmann 2006), and it has been hypothesized that they are important for binding disparate visual objects into unified perceptual constructs (Kreiter and Singer 1996). In the olfactory system, synchronous activity defines odor-specific neural assemblies (Laurent 1996), and olfactory bulb neurons have been shown to synchronize to common inputs *in vitro* (Galan et al. 2006). *In vivo* odor-evoked synchronization and behavioral odor discrimination was impaired by a GABA<sub>A</sub> receptor antagonist (Stopfer et al. 1997). High thresholds that dynamically adapt to the stimulus ensemble have also been observed in visual cortex neurons and hypothesized to allow these cells to select out key features of inputs rather than maximize information transmission (Ringach and Malone 2007). Our results suggest that RF size, spike synchrony, gain, and threshold, superficially disparate aspects of neuronal architecture and biophysics, may in fact be intimately linked and that synchronous and asynchronous processing streams may operate in parallel in the nervous system. With the advent of large-scale multi-electrode recording techniques (Gollisch and Meister 2008; Maravall et al. 2007), it is possible to characterize the frequency selectivity of synchronous activity of large populations of neurons. We predict that downstream neurons with large RFs will share the same tuning as the synchronous events observed in their presynaptic neurons, i.e., Y cells (or magnocellular cells) in the LGN will share the same tuning uncovered by analysis of the synchronous activity of retinal ganglion cells.

#### ACKNOWLEDGMENTS

Thanks to B. Doiron, M. J. Chacron, and R. Krahe for useful discussions. Present address of J. Benda: Department Biology II, Ludwig-Maximilians-Universität, Munich, Planegg-Martinsried, Germany.

#### GRANTS

Funding for this research was provided by the Canadian Institute of Health Research to J. W. Middleton, L. Maler, and A. Lontin and the National Sciences and Engineering Research Council to A. Longtin.

## REFERENCES

- Abbott LF, Dayan P.** The effect of correlated variability on the accuracy of a population code. *Neural Comput* 11: 91–101, 1999.
- Alloway KD.** Information processing streams in rodent barrel cortex: the differential functions of barrel and septal circuits. *Cereb Cortex* 18: 979–989, 2008.
- Azouz R, Gray CM.** Dynamic spike threshold reveals a mechanism for synaptic coincidence detection in cortical neurons in vivo. *Proc Natl Acad Sci USA* 97: 8110–8115, 2000.
- Bastian J.** Electrolocation. II. The effects of moving objects and other electrical stimuli on the activities of two categories of posterior lateral line lobe cells in *Apteronotus albifrons*. *J Comp Physiol [A]* 144: 481–494, 1981.
- Benda J, Longtin A, Maler L.** A synchronization-desynchronization code for natural communication signals. *Neuron* 52: 347–358, 2006.
- Berman NJ, Maler L.** Inhibition evoked from primary afferents in the electrosensory lateral line lobe of the weakly electric fish (*Apteronotus leptorhynchus*). *J Neurophysiol* 80: 3173–3196, 1998.
- Berman NJ, Maler L.** Neural architecture of the electrosensory lateral line lobe: adaptations for coincidence detection, a sensory searchlight and frequency-dependent adaptive filtering. *J Exp Biol* 202: 1243–1253, 1999.
- Borst A, Theunissen FE.** Information theory and neural coding. *Nat Neurosci* 2: 947–957, 1999.
- Bruno RM, Sakmann B.** Cortex is driven by weak but synchronously active thalamocortical synapses. *Science* 312: 1622–1627, 2006.
- Carr CE, Maler L, Sas E.** Peripheral organization and central projections of the electrosensory nerves in gymnotiform fish. *J Comp Neurol* 211: 139–153, 1982.
- Chacron MJ.** Nonlinear information processing in a model sensory system. *J Neurophysiol* 95: 2933–2946, 2006.
- Chacron MJ, Doiron B, Maler L, Longtin A, Bastian J.** Non-classical receptive field mediates switch in a sensory neuron's frequency tuning. *Nature* 423: 77–81, 2003.
- Chacron MJ, Maler L, Bastian J.** Electoreceptor neuron dynamics shape information transmission. *Nat Neurosci* 8: 673–678, 2005.
- Chen L, House JL, Krahe R, Nelson ME.** Modeling signal and background components of electrosensory scenes. *J Comp Physiol [A]* 191: 331–345, 2005.
- Cruikshank SJ, Lewis TJ, Connors BW.** Synaptic basis for intense thalamocortical activation of feedforward inhibitory cells in neocortex. *Nat Neurosci* 10: 462–468, 2007.
- Dan Y, Alonso JM, Usrey WM, Reid RC.** Coding of visual information by precisely correlated spikes in the lateral geniculate nucleus. *Nat Neurosci* 1: 501–507, 1998.
- de la Rocha J, Parga N.** Short-term synaptic depression causes a non-monotonic response to correlated stimuli. *J Neurosci* 25: 8416–8431, 2005.
- Destexhe A, Rudolph M, Pare D.** The high-conductance state of neocortical neurons in vivo. *Nat Rev* 4: 739–751, 2003.
- Doiron B, Laing C, Longtin A, Maler L.** Ghostbursting: a novel neuronal burst mechanism. *J Comput Neurosci* 12: 5–25, 2002.
- Doiron B, Oswald AM, Maler L.** Interval coding. II. Dendrite-dependent mechanisms. *J Neurophysiol* 97: 2744–2757, 2007.
- Ellis LD, Krahe R, Bourque CW, Dunn RJ, and Chacron MJ.** Muscarinic receptors control frequency tuning through the downregulation of an A-type potassium current. *J Neurophysiol* 98: 1526–1537, 2007.
- Ellis LD, Maler L, Dunn RJ.** Differential distribution of SK channel subtypes in the brain of the weakly electric fish *Apteronotus leptorhynchus*. *J Comp Neurol* 507: 1964–1978, 2008.
- Foffani G, Chapin JK, Moxon KA.** Computational role of large receptive fields in the primary somatosensory cortex. *J Neurophysiol* 100: 268–280, 2008.
- Galan RF, Fourcaud-Trocme N, Ermentrout GB, Urban NN.** Correlation-induced synchronization of oscillations in olfactory bulb neurons. *J Neurosci* 26: 3646–3655, 2006.
- Gollisch T, Meister M.** Rapid neural coding in the retina with relative spike latencies. *Science* 319: 1108–1111, 2008.
- Heiligenberg W, Dye J.** Labelling of electroreceptive afferents in a gymnotoid fish by intracellular injection of HRP: the mystery of multiple maps. *J Comp Physiol [A]* 148: 287–296, 1982.
- Kaplan E, Shapley RM.** X and Y cells in the lateral geniculate nucleus of macaque monkeys. *J Physiol* 330: 125–143, 1982.
- Krahe R, Bastian J, Chacron MJ.** Temporal processing across multiple topographic maps in the electrosensory system. *J Neurophysiol* 100: 852–867, 2008.
- Kreiter AK, Singer W.** Stimulus-dependent synchronization of neuronal responses in the visual cortex of the awake macaque monkey. *J Neurosci* 16: 2381–2396, 1996.
- Laurent G.** Dynamical representation of odors by oscillating and evolving neural assemblies. *Trends Neurosci* 19: 489–496, 1996.
- Lewis JE, Maler L.** Neuronal population codes and the perception of object distance in weakly electric fish. *J Neurosci* 21: 2842–2850, 2001.
- Maler L, Finger T, Karten HJ.** Differential projections of ordinary lateral line receptors and electroreceptors in the gymnotoid fish, *Apteronotus (Ster-narchus) albifrons*. *J Comp Neurol* 158: 363–382, 1974.
- Maler L, Mugnaini E.** Correlating gamma-aminobutyric acidergic circuits and sensory function in the electrosensory lateral line lobe of a gymnotiform fish. *J Comp Neurol* 345: 224–252, 1994.
- Malone BJ, Kumar VR, Ringach DL.** Dynamics of receptive field size in primary visual cortex. *J Neurophysiol* 97: 407–414, 2007.
- Maravall M, Petersen RS, Fairhall AL, Arabzadeh E, Diamond ME.** Shifts in coding properties and maintenance of information transmission during adaptation in barrel cortex. *PLoS Biol* 5: e19, 2007.
- Mehaffey WH, Doiron B, Maler L, Turner RW.** Deterministic multiplicative gain control with active dendrites. *J Neurosci* 25: 9968–9977, 2005.
- Mehaffey WH, Maler L, Turner RW.** Intrinsic frequency tuning in ELL pyramidal cells varies across electrosensory maps. *J Neurophysiol* 99: 2641–2655, 2008.
- Metzner W, Juraneck J.** A sensory brain map for each behavior? *Proc Natl Acad Sci USA* 94: 14798–14803, 1997.
- Middleton JW, Longtin A, Benda J, Maler L.** The cellular basis for parallel neural transmission of a high-frequency stimulus and its low-frequency envelope. *Proc Natl Acad Sci USA* 103: 14596–14601, 2006.
- Oswald AM, Chacron MJ, Doiron B, Bastian J, Maler L.** Parallel processing of sensory input by bursts and isolated spikes. *J Neurosci* 24: 4351–4362, 2004.
- Papoulis A, Pillai SU.** *Probability, Random Variables and Stochastic Processes*. New York: McGraw-Hill, 2002.
- Rice SO.** *Mathematical Analysis of Random Noise*. New York: Dover, 1954.
- Ringach DL, Malone BJ.** The operating point of the cortex: neurons as large deviation detectors. *J Neurosci* 27: 7673–7683, 2007.
- Roddey JC, Girish B, Miller JP.** Assessing the performance of neural encoding models in the presence of noise. *J Comput Neurosci* 8: 95–112, 2000.
- Salinas E, Sejnowski TJ.** Impact of correlated synaptic input on output firing rate and variability in simple neuronal models. *J Neurosci* 20: 6193–6209, 2000.
- Senn W, Segev I, Tsodyks M.** Reading neuronal synchrony with depressing synapses. *Neural Comput* 10: 815–819, 1998.
- Shumway CA.** Multiple electrosensory maps in the medulla of weakly electric gymnotiform fish. I. Physiological differences. *J Neurosci* 9: 4388–4399, 1989.
- Shumway CA, Maler L.** GABAergic inhibition shapes temporal and spatial response properties of pyramidal cells in the electrosensory lateral line lobe of gymnotiform fish. *J Comp Physiol [A]* 164: 391–407, 1989.
- Softky WR, Koch C.** The highly irregular firing of cortical cells is inconsistent with temporal integration of random EPSPs. *J Neurosci* 13: 334–350, 1993.
- Stopfer M, Bhagavan S, Smith BH, Laurent G.** Impaired odour discrimination on desynchronization of odor-encoding neural assemblies. *Nature* 390: 70–74, 1997.
- Wang D, Maler L.** The immunocytochemical localization of glutamate in the electrosensory system of the gymnotiform fish, *Apteronotus leptorhynchus*. *Brain Res* 653: 215–222, 1994.
- Wässle H.** Parallel processing in the mammalian retina. *Nat Rev* 5: 747–757, 2004.
- Wehr M, Zador AM.** Balanced inhibition underlies tuning and sharpens spike timing in auditory cortex. *Nature* 426: 442–446, 2003.
- Weng C, Yeh CI, Stoelzel CR, Alonso JM.** Receptive field size and response latency are correlated within the cat visual thalamus. *J Neurophysiol* 93: 3537–3547, 2005.
- Zhang K, Sejnowski TJ.** Neuronal tuning: To sharpen or broaden? *Neural Comput* 11: 75–84, 1999.